Advancing Autonomous Navigation: Near-Moon GNSS-based Orbit Determination

Advancing Autonomous Navigation: Near-Moon GNSS-based Orbit Determination

Oliviero Vouch[1], Andrea Nardin[1], Alex Minetto[1], Simone Zocca[1], Fabio Dovis[1], Lauren Konitzer[2], Joel J.K. Parker[2], Benjamin Ashman[2], Fabio Bernardi[3], Simone Tedesco[3], Samuele Fantinato[3], and Claudia Facchinetti[4]

[1]*Department of Electronics and Telecommunications (DET), Politecnico di Torino, Torino, Italy*
[2]*NASA Goddard Space Flight Center, Greenbelt, Maryland, USA*
[3]*Qascom SRL, Bassano del Grappa, Vicenza, Italy*
[4]*Italian Space Agency (ASI–Agenzia Spaziale Italiana), Roma, Italy*

BIOGRAPHY

Oliviero Vouch is a Ph.D. student working with the Navigation Signal Analysis and Simulation (NavSAS) group. His research interests cover advanced Bayesian estimation applied to multi-sensor integrated navigation units based on Global Navigation Satellite System (GNSS).

Andrea Nardin is Assistant Professor at the Department of Electronics and Telecommunications of Politecnico di Torino where he has been working with the NavSAS group since 2018. His research interests include signal processing architectures and signal design applied to GNSSs and LEO PNT.

Alex Minetto joined the Department of Electronics and Telecommunications of Politecnico di Torino, in 2021 as a Researcher and Assistant Professor. His current research interests cover navigation signal design and processing, advanced Bayesian estimation applied to positioning, navigation, and timing technologies.

Simone Zocca is a Ph.D. student within the NavSAS group at the Department of Electronics and Telecommunications of Politecnico di Torino. His research is focused on innovative solutions for signal processing techniques and Bayesian estimation applied to Global Navigation Satellite System (GNSS).

Fabio Dovis is Full Professor at the Department of Electronics and Telecommunications, Politecnico di Torino. He coordinates the NavSAS Group and is Co-PI of the LuGRE project. His research interests include design of GPS and Galileo receivers and advanced signal processing for interference and multipath detection and mitigation, and also ionospheric monitoring.

Lauren Konitzer is a Navigation and Mission Design Engineer at NASA Goddard Space Flight Center. She is the Deputy Principal Investigator for the Lunar GNSS Receiver Experiment (LuGRE).

Joel J.K. Parker is a Senior Navigation Engineer in the Navigation and Mission Design Branch at NASA GSFC. He is the LuGRE Principal Investigator (PI).

Benjamin Ashman is a Navigation Engineer in the Navigation and Mission Design Branch at NASA GSFC, and was the 2021–2022 ION/AAAS Congressional Science and Engineering Fellow. He is a member of the LuGRE PI team.

Fabio Bernardi is a Radio Navigation Engineer in the Advanced Navigation Unit at Qascom. He is involved in the LuGRE payload.

Simone Tedesco is a Radio Navigation Engineer in the Advanced Navigation Unit at Qascom. He is involved in the LuGRE payload.

Samuele Fantinato is Head of the Advanced Navigation Unit at Qascom. He is Program/Project Manager (PM) of the LuGRE payload.

Claudia Facchinetti leads the Engineering, Cost Analysis & CEF Office within the Engineering and Future Space Systems Unit at ASI. She is the Agenzia Spaziale Italiana (ASI–Italian Space Agency) Project Manager of the LuGRE Payload.

ABSTRACT

Global Navigation Satellite Systems (GNSSs) have settled as a crucial asset for Positioning, Navigation and Timing (PNT) within the Space Service Volume (SSV), and this technology is increasingly recognized a major player to serve the realm of lunar exploration missions. Current space operations are heavily relying on ground infrastructures, with escalating operational costs and limited resources. Therefore, it is urgent to enhance autonomy of space users, particularly in the task of real-time Orbit Determination (OD). This study aims to demonstrate the performance of GNSS-based onboard OD in the lunar regime. In a sequential Bayesian architecture, where GNSS observations are filtered with an orbital propagator, the sigma-point Unscented

Kalman Filter (UKF) model is compared against the renowned Extended Kalman Filter (EKF)-based Orbital Filter (OF). The upcoming LuGRE mission serves as a case study, showcasing near-Moon PNT from a simulated portion of lunar ignition orbit at approximately 61 Earth Radii (RE). Both navigation algorithms are assessed with actual receiver observables, retrieved from a high-fidelity Hardware-in-the-Loop (HIL) simulation. Results highlight that the UKF effectively smooths out harmful Dilution of Precision (DOP) leaps induced by losses of lock of some GNSS signals, while maintaining position estimation errors within 2 km for 98.97% of the time. Moreover, remarkable accuracy gains over the EKF are observed, with a 3σ percentile improvement of 79.97% for position estimates and 63.62% for velocity estimates.

I. INTRODUCTION

In contemporary space operations, the navigation, guidance, and maneuvering of space vehicles largely depend on ground segment assets. Radio Frequency (RF) tracking via Deep Space Networks (DSNs) facilities and Direct-to-Earth (DTE) links enables advanced Orbit Determination (OD) techniques through sophisticated off-board processing algorithms (Iess et al., 2014). However, relying on ground-segment assets introduces several drawbacks. Operational costs are elevated, and the management of numerous missions is constrained by limited ground segment resources (Turan et al., 2022). To meet the objectives set by the space exploration roadmap, there is a pressing need to enhance autonomous navigation capabilities.

In the Space Service Volume (SSV), Global Navigation Satellite Systems (GNSSs) are a crucial asset for autonomous spacecraft (S/C) navigation and timing, and their usage has been regulated up to Geosynchronous Orbit (GEO) altitudes (Parker et al., 2018). While processing of Earth's GNSS signal in space has been proven feasible at higher altitudes, several technological challenges arise. The Earth's obstruction of satellite signals determines drops of availability. Moreover, the increased free-space path loss attenuation together with frequent tracking of side lobes results in weak signal reception and noisy observations. Additionally, the unfavourable geometric diversity of ranging sources can exacerbate navigation uncertainty.

Targeting the lunar regime, scientific literature has proposed sequential filtering architectures to address the challenges of ground-independent and precise OD using onboard GNSS radiometric observations. Extended Kalman Filter (EKF)-based Orbital Filter (OF) models, as pioneered by (Capuano, 2016), have demonstrated significant navigation performance in Earth-Moon transfer orbit (MTO) up to Moon altitudes. In line with the reduced dynamic approach, (Capuano et al., 2017) augmented the state space model with pseudo-stochastic parameters to mitigate the effects of unmodeled or mismodeled S/C dynamics. Additionally, an ensemble Kalman filter (EnKF) model targeting orbital navigation in MTO has shown promising performance in simulations at lunar altitudes (Murata, 2023). Recently, unconventional EKF architectures that constrain a kinematic OD solution with a planned orbital trajectory have also been proposed (Vouch et al., 2024).

As part of National Aeronautics and Space Administration (NASA)'s Commercial Lunar Payload Services (CLPS) program (Task Order 19D), the Lunar GNSS Receiver Experiment (LuGRE) (Parker et al., 2022) serves as case study to investigate the potential of more advanced Bayesian formulations for autonomous GNSS-based orbital navigation of a S/C in lunar proximity. The LuGRE technology development payload will deploy the Navigation Early Investigation on Lunar surface (NEIL) module–a GNSS Software Defined Radio (SDR) receiver specifically customized for operations in deep-space (Tedesco et al., 2023)– onboard the US Firefly Blue Ghost Mission 1 (BGM1) lander. The mission aims to be the first flight demonstration of multi-GNSS PNT in cis-lunar space and on the Moon surface; one of the key scientific objectives of LuGRE is to assess the performance of filtering-based PNT solutions obtained both by the real-time receiver operation and through ground-based post-processing of sampled multi-system, multi-band observables (Minetto et al., 2022; Nardin et al., 2022, 2023).

This work explores the potential of a more complex Unscented Kalman Filter (UKF) model which integrates multi-channel GNSS observables tightly with the prediction of space dynamics from an orbital propagator. Benchmarking the UKF formulation against an EKF-based model, a Low Lunar Orbit (LLO) segment 61 RE away from Earth is considered to comprehensively assess the attainable orbital navigation performance. In particular, both Bayesian estimators are tested for the post-processing of observables constructed by the LuGRE receiver in a Hardware-in-the-Loop (HIL) simulation with RF GNSS signals. Leveraging a faithful model for the RF link simulation, the operational environment seen by a receiver in lunar proximity is also discussed in terms of navigation metrics. Even with an error-prone initialization, the UKF-based architecture can effectively tackle harsh multilateration geometry and reduced availability exhibiting position estimation errors within 2 km for the 98.97% of the analyzed orbit.

II. BACKGROUND

From the navigation perspective, OD is the problem of determining the S/C motion relative to the center of mass of the Earth, and express it in a specified coordinate system. Orbital motion is described by the state of the dynamical system, which encompasses the instantaneous S/C position and velocity as minimal set of parameters useful to predict future motion states. In a Bayesian filtering framework, GNSS-based orbital navigation can be framed as a statistical estimation process which sequentially estimates the belief of the latent system state. Given an initial estimate $\boldsymbol{x}_0$ of the state drawn from a distribution

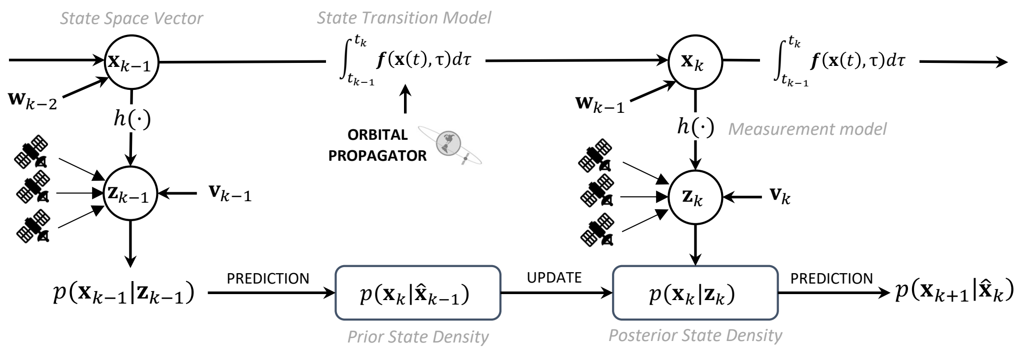

Figure 1: Bayesian filtering approach for orbital navigation with radiometric GNSS observations, integrating predictions from an orbital propagation model. Inspired by (Fang et al., 2018).

$p(\boldsymbol{x}_0)$ which reflects the initial knowledge about the system (i.e., the initial condition), the estimation process tackled by the Bayesian filter follows two steps:

- **Prediction of the prior state density**: the moments of the prior $p(\mathbf{x}_k|\hat{\mathbf{x}}_{k-1})$[1] predict the system state evolution at time t_k by applying the transitional model $\boldsymbol{f}(\cdot)$ to the latest state estimate $\hat{\mathbf{x}}_{k-1}$.
- **Estimation of the posterior state density**: the posterior $p(\mathbf{x}_k|\mathbf{z}_k)$ is estimated leveraging sampled observations $\mathbf{z}_k$ which relate to the state through the measurement model $\boldsymbol{h}(\cdot)$.

A mathematical formulation of the S/C orbital dynamics (i.e., an *orbital propagator*) defines the transitional (or, motion) model as a non-linear, stochastic differential equation:

$$\dot{\boldsymbol{x}}(t) = \boldsymbol{f}(\boldsymbol{x}(t), t) + \boldsymbol{w}(t)\ . \tag{1}$$

Inaccuracies in the physical model of the orbital forces would end up causing the orbital propagator to deviate from the actual motion. These effects, together with deterministic yet unknown control inputs, are captured in the process noise term $\boldsymbol{w}(t)$. As a matter of fact, (1) is a transitional model with continuous-time dynamics. Although the orbital motion is more accurately described in continuous-time, the system is observed at discrete-time instants. When an estimate of the orbiting vehicle state is available at t_{k-1}, (1) can be numerically integrated (cf. (Battin, 1999)) between sample intervals:

$$\boldsymbol{x}_k = \boldsymbol{x}_{k-1} + \int_{t_{k-1}}^{t_k} \boldsymbol{f}(\boldsymbol{x}(t), \tau) d\tau + \boldsymbol{w}_k\ . \tag{2}$$

Model (2) characterizes the system evolution in terms of an equivalent non-linear, discrete-time difference equation. The random white-noise sequence $\boldsymbol{w}_k$ is considered from the discretization of a piecewise constant process noise (Schutz et al., 2004). Under the assumption that the system state evolves as a discrete-time Markov process, a graphical representation of the sequential procedure is shown in Figure 1.

When sampled GNSS observations are retrieved onboard (i.e., $\boldsymbol{z}_k$), they are processed through the measurement model:

$$\boldsymbol{z}_k = \boldsymbol{h}_k(\boldsymbol{x}_k) + \boldsymbol{v}_k\ . \tag{3}$$

This model filters observations using predictions based on orbital propagation, treating non-systematic measurement errors as additive disturbances with runtime-adaptable covariance. The resulting Bayesian formulation integrates GNSS observables tightly with the prediction of space dynamics (Capuano, 2016). This approach is well-suited at lunar altitudes where GNSS signal depletion occurs and blind spots are likely to intermittently appear. In fact, the integration of an orbital propagator enables continuous navigation without the need for a minimum set of radiometrically visible satellites to compute a single-point solution. Additionally, a limited number of measurements can still be beneficial in constraining the model-based orbital propagation, provided these measurements are not outliers. This helps to prevent drift caused by the integration of process noise.

[1] $\boldsymbol{x}_k = \boldsymbol{x}\,(t = t_k)$, and $\hat{\boldsymbol{x}}_k$ is an estimate of the true yet unknown system state.

1. Space vehicle dynamics

In the framework of Newtonian's physics, the S/C motion dynamics in an inertial reference frame relative to the Earth's center of mass are governed by the two-body model:

$$\ddot{\boldsymbol{r}}(t) = -\frac{GM_e\boldsymbol{r}(t)}{r(t)^3} = -\frac{\mu_e\boldsymbol{r}(t)}{r(t)^3} \tag{4}$$

which defines the second-order differential equation of motion for the unperturbed Keplerian orbit. In particular:

- $\boldsymbol{r}(t) = [r_x(t), r_y(t), r_z(t)]^T$ is the instantaneous, absolute S/C position vector expressed in an Earth-Centered Inertial (ECI) reference frame (or, its realization in the J2000 frame);
- $\dot{\boldsymbol{r}}(t) = [\dot{r}_x(t), \dot{r}_y(t), \dot{r}_z(t)]^T$ is the instantaneous, absolute S/C velocity vector expressed in ECI frame;
- $\ddot{\boldsymbol{r}}(t) = [\ddot{r}_x(t), \ddot{r}_y(t), \ddot{r}_z(t)]^T$ is the instantaneous, absolute S/C acceleration vector expressed in ECI frame;
- $r(t)$ is the instantaneous geocentric distance of the S/C from the Earth center of mass (i.e., $r(t) = \|\boldsymbol{r}(t)\|$)
- μ_e is the Earth's gravitational parameter ($\mu_e = 398600.4405\ \mathrm{km}^3\,\mathrm{s}^{-2}$ based on (Montenbruck et al., 2002))

Time is the independent variable in the equations of motion for orbital navigation using GNSS measurements, which are tagged to the GPS Time (GPST). Transformations using International Atomic Time (TAI) are needed for transitions between dynamical and atomic time scales (Montenbruck et al., 2002). However, time dependence will be implicit hereafter and time variable will be omitted.

It is remarked that (4) undertakes the assumption of the Earth being a sphere that is gravitationally equivalent to point mass. Although a realistic Earth's gravitation model should account for the geopotential gradient due to the non-uniform mass distribution of the geoid, this first-order approximation is increasingly acceptable for orbital altitudes above $50\,000\ \mathrm{km}$ (Montenbruck et al., 2002). As the S/C moves away from the Earth in the interplanetary trajectory towards the Moon, other perturbing forces become dominant, such as luni-solar gravitational fields and solar radiation pressure (SRP). Incorporating third-body effects into the S/C's orbital dynamics extends the two-body model into a multi-body problem. Since the physical realization of forces is additive in nature, the non-linear differential equation of perturbed orbital motion can be expressed following Cowell's formulation:

$$\ddot{\boldsymbol{r}} = -\frac{\mu_e\boldsymbol{r}}{r^3} + \ddot{\boldsymbol{r}}_p\ . \tag{5}$$

The net perturbative acceleration $\ddot{\boldsymbol{r}}_p$ to the spherically symmetric Earth's gravitation reads as:

$$\ddot{\boldsymbol{r}}_p = \ddot{\boldsymbol{r}}_{3b} + \ddot{\boldsymbol{r}}_{srp} \tag{6}$$

and it includes $\ddot{\boldsymbol{r}}_{3b}$ the acceleration due to the point mass gravitation of other celestial bodies, and $\ddot{\boldsymbol{r}}_{srp}$ the acceleration arising from solar photons impinging on the S/C surface.

Assuming a set of n_c celestial bodies, the first term of (6), resolved about ECI frame axes, is:

$$\ddot{\boldsymbol{r}}_{3b} = \sum_{j=1}^{n_c} \mu_j \left(\frac{\boldsymbol{r}_j - \boldsymbol{r}}{\|\boldsymbol{r}_j - \boldsymbol{r}\|^3} - \frac{\boldsymbol{r}_j}{r_j^3} \right)\ . \tag{7}$$

where $\boldsymbol{r}_j$ denotes the geocentric position vector of the j-th celestial body, r_j its distance from the Earth's center of mass, and μ_j its planetary mass parameter. For GNSS-based navigation in deep-space up to cislunar altitudes and lunar orbits, (7) encompasses perturbations from the Sun and Moon. The geocentric positions of these celestial bodies can be retrieved from Jet Propulsion Laboratory (JPL) Development Ephemerides series DE440 (Park et al., 2021). These ephemerides, reference to the International Celestial Reference System (ICRS) (e.g., ECI-frame), and are computed by fitting integrated orbits to both ground-based and space-based observations in a series of Chebyshev polynomials. The DE series are time-tagged to Barycentric Coordinate Time (TCB), requiring conversions to align with GPST. The planetary mass parameters according to DE440 are tabulated in (Park et al., 2021).

The SRP induced acceleration on a S/C of mass m can be considered as a surface force which is approximated by the following spherical model (McMahon, 2011):

$$\ddot{\boldsymbol{r}}_{srp} = -P_{srp}^{1\mathrm{AU}} \left(\frac{1\mathrm{AU}}{\|\boldsymbol{r}_s - \boldsymbol{r}\|} \right)^2 \frac{A}{m} C_R \frac{\boldsymbol{r}_s - \boldsymbol{r}}{\|\boldsymbol{r}_s - \boldsymbol{r}\|} \tag{8}$$

where A is the S/C exposed area to solar energy, C_R is the radiation pressure coefficient (cf. Table 3.5 of (Montenbruck et al., 2002)) that depends on the S/C reflectivity ϵ, and $\boldsymbol{r}_s$ is the ECI-frame position vector of the Sun. Assuming that A absorbs all photons (i.e., $\epsilon = 0$) and is normal to the direction of the incoming radiation, $P_{srp}^{1\mathrm{AU}} \approx 4.56 \times 10^{-6}\ \mathrm{N\,m^{-2}}$ is the force of solar pressure per unit area in one astronomical distance ($1\mathrm{AU} \approx 149.6 \times 10^{6}\ \mathrm{km}$).

Building upon (1), the orbital dynamic model in an ECI-frame can be obtained as a variation of Cowell's formulation (6) into a non-linear, first-order vector differential equation:

$$\frac{d}{dt}\underbrace{\begin{bmatrix}\boldsymbol{r}\\ \dot{\boldsymbol{r}}\end{bmatrix}}_{\boldsymbol{x}^{sc}} = \underbrace{\begin{bmatrix}\dot{\boldsymbol{r}}\\ -\frac{\mu_e \boldsymbol{r}}{r^3} + \ddot{\boldsymbol{r}}_{3b} + \ddot{\boldsymbol{r}}_{srp}\end{bmatrix}}_{\boldsymbol{f}(\boldsymbol{x}^{sc},t)} + \begin{bmatrix}\boldsymbol{0}_{3\times 1}\\ \boldsymbol{w}^{sc}\end{bmatrix} \tag{9}$$

where $\boldsymbol{w}^{sc}$ is the instantaneous acceleration driving noise with Power Spectral Density (PSD) $\boldsymbol{S}_{\boldsymbol{w}}^{sc} = \left[S_{w_x}^{sc},\, S_{w_y}^{sc},\, S_{w_z}^{sc}\right]^T$.

The differential model (9) is applicable for a deep-space orbital propagator during a transfer orbit above $50\,000\ \mathrm{km}$ altitude, and it is also suitable for cislunar and lunar altitudes. Recent contributions have considered a model in a selenocentric inertial frame that incorporates higher-order lunar gravity harmonics (Iiyama et al., 2024). Nonetheless, this model lies beyond the scope of the present study.

2. GNSS measurement model and clock dynamics

Sampled GNSS observations admit a non-linear functional model with the S/C positioning states. Assuming Time-Of-Arrival (TOA) ranging based on code tracking, the pseudorange equation for the PRN sequence transmitted by the i-th GNSS satellite is formulated at time t_k as:

$$\rho_k^i = \left\|\boldsymbol{r}_k - \boldsymbol{r}_k^i\right\| + c \cdot \delta t_{u,k} + \epsilon_k^i \tag{10}$$

where:

- $\boldsymbol{r}_k^i$ is the position vector of the satellite center of mass at t_k;
- $\delta t_{u,k}$ is the receiver clock offset relative to GNSS system time at t_k;
- ϵ_k^i is the non-systematic, residual model error which combines both signal-in-space user range error (SISRE) and user equipment error (UEE) into the user equivalent range error (UERE) (Teunissen and Montenbruck, 2017).

The pseudorange equation (10) is valid under the assumption that space-segment corrections, relativistic effects, atmospheric delays[2], and biases have been compensated for by external data or physical models (Teunissen and Montenbruck, 2017). The position vector $\boldsymbol{r}_k$ is referenced to the phase center of the GNSS receiver antenna onboard the S/C, unlike Section II.1, which considers the position relative to the S/C center of gravity. A lever-arm correction factor should be applied to account for such spatial offset. For a GNSS receiver tracking PRN sequences of both GPS and Galileo satellites, $\delta t_{u,k}$ represents the clock-offset relative to GPST. As such, the Galileo pseudorange equation must include an additional term for the GPS-to-Galileo time-offset (GGTO). This GGTO can either be obtained from the navigation message and applied as a space-segment correction or, if not demodulated, included as an unknown parameter in the sequential estimation process. The former approach is considered in the observation model formulation according to Section II.3. Moreover, the satellite position vector in (10), whether computed from broadcast ephemeris parameters in the navigation message or through precise orbit products, is determined in an Earth-Centered Earth-Fixed (ECEF) frame (i.e., WGS84) (Teunissen and Montenbruck, 2017). Since the receiver position vector is more conveniently expressed in an ECI frame, a rotational transformation is required to compare on-board GNSS measurements with satellite positions.

Doppler measurements arise from the relative motion between the receiver and GNSS satellites, and they are relevant to the estimation of both the receiver velocity and the frequency deviation of the receiver clock. The Doppler model can be derived by differentiating the pseudorange equation with respect to time, and is computed from the projection of the relative satellite-receiver velocity vector onto the receiver-to-satellite Line-of-Sight (LOS) (Morichi et al., 2024). For the tracked carrier component of the i-th GNSS satellite, the Doppler measurement D_k^i is expressed as:

$$\underbrace{\dot{\rho}_k^i - \dot{\boldsymbol{r}}_k^i \cdot \boldsymbol{e}_k^i}_{D_k^i} = -\boldsymbol{e}_k^i \cdot \dot{\boldsymbol{r}}_k + c \cdot \delta\dot{t}_{u,k} + \dot{\epsilon}_k^i \tag{11}$$

[2] When tracking signals on multiple frequency bands, the dispersive group delay induced by the ionosphere is referenced to a single frequency using frequency-dependent ionospheric coefficients.

where:

- $\dot{\rho}_k^i$ is the pseudorange-rate measurement at t_k;
- $\dot{\boldsymbol{r}}_k^i$ is the velocity vector of the satellite center of mass at t_k;
- $\boldsymbol{e}_k^i = \left[e_{x,k}^i,\, e_{y,k}^i,\, e_{z,k}^i\right]^T$ is the unit pointing vector from the S/C position to i-th satellite position at t_k;
- $\delta\dot{t}_{u,k}$ is the receiver oscillator frequency deviation (i.e., clock drift);
- $\dot{\epsilon}_k^i$ is the residual error after model-based corrections and compensation of known physical effects.

Eventually, clock dynamics can be modelled using to the following discrete-time, linear stochastic system (Galleani, 2008):

$$\underbrace{\begin{bmatrix}\delta t_{u,k}\\ \delta\dot{t}_{u,k}\end{bmatrix}}_{\boldsymbol{x}_k^{clk}} = \underbrace{\begin{bmatrix}1 & \Delta t\\ 0 & 1\end{bmatrix}}_{\boldsymbol{\Phi}^{clk}} \begin{bmatrix}\delta t_{u,k-1}\\ \delta\dot{t}_{u,k-1}\end{bmatrix} + \underbrace{\begin{bmatrix}w_{\phi,k}^{clk}\\ w_{f,k}^{clk}\end{bmatrix}}_{\boldsymbol{w}_k^{clk}} \tag{12}$$

where $\Delta t = t_k - t_{k-1}$, $\boldsymbol{\Phi}^{clk}$ is the time-invariant state-transition matrix, and $\boldsymbol{w}_k^{clk}$ is the white noise random sequence (i.e., from discretization of clock noise random walk) with stationary covariance $\boldsymbol{Q}^{clk}$ (cf. Section 9.3 in (Brown and Hwang, 1992)).

3. State-space model formulation

Combining S/C orbital dynamics with the GNSS receiver clock states, the state vector for GNSS-based orbital navigation can be defined at time t_k:

$$\boldsymbol{x}_k = \left[\boldsymbol{x}_k^{sc^T}\ \boldsymbol{x}_k^{clk^T}\right]^T \in \mathbb{R}^{n\times 1} \tag{13}$$

where $\boldsymbol{x}_k^{sc} \in \mathbb{R}^{6\times 1}$ includes the S/C absolute position and velocity vector states at time t_k, and $n = 8$ for the present study. Starting from the non-linear, differential model (9) for perturbed orbital motion, an approximate linear model between sample times can be derived by linearizing around the latest estimate of S/C dynamics (i.e., $\hat{\boldsymbol{x}}_{k-1}^{sc}$). The solution to the first-order, vector differential equation of the state-transition matrix can be expressed as a function of the system matrix (Bar-Shalom et al., 2004):

$$\boldsymbol{\Phi}_{k-1,k}^{sc} = e^{\boldsymbol{F}^{sc}\left(t,\hat{\boldsymbol{x}}_{k-1}^{sc}\right)\Delta t} \tag{14}$$

where:

$$\boldsymbol{F}^{sc}\left(t,\hat{\boldsymbol{x}}_{k-1}^{sc}\right) = \left.\frac{\partial \boldsymbol{f}\left(\boldsymbol{x}^{sc},t\right)}{\partial \boldsymbol{x}^{sc}}\right|_{\boldsymbol{x}^{sc}=\hat{\boldsymbol{x}}_{k-1}^{sc}} = \begin{bmatrix}\boldsymbol{0}_{3\times 3} & \boldsymbol{I}_{3\times 3}\\ \frac{\partial}{\partial \boldsymbol{r}}\left(-\frac{\mu_e \boldsymbol{r}}{r^3} + \ddot{\boldsymbol{r}}_{3b} + \ddot{\boldsymbol{r}}_{srp}\right)\Big|_{\boldsymbol{x}^{sc}=\hat{\boldsymbol{x}}_{k-1}^{sc}} & \boldsymbol{0}_{3\times 3}\end{bmatrix}. \tag{15}$$

The partial derivatives of Earth's point mass gravitation, third-body effects, and SRP can be found in (Montenbruck et al., 2002). From (14), the state-transition matrix for the linearized dynamics is obtained via Taylor series approximation. The linearized approximation may be inaccurate compared to the true transition matrix. An alternative is to express the differential equation of the state-transition matrix in variational form, and use numerical integration (Montenbruck et al., 2002). A simpler approach is to use a complex-step derivative approximation (Capuano, 2016).

Assuming a first-order Taylor approximation of (14), the state-transition matrix including receiver clock states takes the form:

$$\boldsymbol{\Phi}_{k-1,k} = \begin{bmatrix}\boldsymbol{I}_{6\times 6} + \boldsymbol{F}^{sc}\left(t,\hat{\boldsymbol{x}}_{k-1}^{sc}\right)\Delta t & \boldsymbol{0}_{6\times 2}\\ \boldsymbol{0}_{2\times 6} & \boldsymbol{\Phi}^{clk}\end{bmatrix}. \tag{16}$$

Discretizing the process driving noise in (9) into a white noise sequence $\boldsymbol{w}_k^{sc}$, the covariance matrix of the discrete process sequence affecting state-transition dynamics becomes:

$$\boldsymbol{Q}_k = \begin{bmatrix}\boldsymbol{Q}_k^{sc} & \boldsymbol{0}_{6\times 2}\\ \boldsymbol{0}_{2\times 6} & \boldsymbol{Q}^{clk}\end{bmatrix},\quad \boldsymbol{Q}_k^{sc} = \begin{bmatrix}\frac{\Delta t^3}{3} & \frac{\Delta t^2}{2}\\ \frac{\Delta t^2}{2} & \Delta t\end{bmatrix} \otimes \operatorname{diag}\left(\boldsymbol{S}_{\boldsymbol{w}_k}^{sc}\right) \tag{17}$$

where $\boldsymbol{S}_{\boldsymbol{w}_k}^{sc} = \left[S_{w_x,k}^{sc},\, S_{w_y,k}^{sc},\, S_{w_z,k}^{sc}\right]^T$ is the sampled PSD of the acceleration process white noise.

In a similar vein, the non-linear GNSS observation model (cf. Section II.2) can be linearized by taking the partials of the measurements about the state evaluated locally at the sample instant. Assuming N_s tracked GPS/Galileo satellites at time t_k and GGTO demodulation (i.e., single constellation model), the Jacobian of the observation equations (10) and (11) is computed as:

$$\boldsymbol{H}_k = \begin{bmatrix} \tilde{\boldsymbol{H}}_k & \mathbf{0}_{N_s \times 3} & c \cdot \mathbf{1}_{N_s \times 1} & \mathbf{0}_{N_s \times 1} \\ \mathbf{0}_{N_s \times 3} & \tilde{\boldsymbol{H}}_k & \mathbf{0}_{N_s \times 1} & c \cdot \mathbf{1}_{N_s \times 1} \end{bmatrix} , \quad \tilde{\boldsymbol{H}}_k = \begin{bmatrix} -\boldsymbol{e}_k^1, \; \ldots, \; -\boldsymbol{e}_k^{N_s} \end{bmatrix}^T . \tag{18}$$

This linearized measurement model is valid under the assumption of processing single-frequency, code-based observations. For dual-frequency processing, (18) strictly holds after ionosphere-free linear combination (Teunissen and Montenbruck, 2017).

When considering the processing of GNSS observations in a Kalman-based estimator, measurement noise $\boldsymbol{v}_k$ is modeled as a white random sequence with non-stationary covariance $\boldsymbol{R}_k$. The latter assumption is reasonable given the highly-variable GNSS signal characteristics as a function of the S/C altitude, and thus over time. For N_s pseudorange and pseudorange-rate observations available from navigation satellites, the covariance matrix is compactly written as:

$$\boldsymbol{R}_k = \mathrm{diag}\left(\left[\sigma^2_{\epsilon_k^{1,S}}, \; \ldots, \; \sigma^2_{\epsilon_k^{N_s,S}}, \; \sigma^2_{\dot{\epsilon}_k^{1,S}}, \; \ldots, \; \sigma^2_{\dot{\epsilon}_k^{N_s,S}} \right] \right) . \tag{19}$$

For the stochastic disturbance affecting pseudorange observations, the error budget in terms of UERE includes space-segment errors (i.e., satellite clock and ephemeris parameters), uncorrected atmospheric effects, relativistic errors, and receiver noise. The dominant contributor to receiver noise on pseudorange measurements is the code tracking jitter from the Delay-Lock Loop (DLL), induced by thermal noise. The model from (Betz and Kolodziejski, 2000), valid for BPSK modulated codes[3], can be used to weight code tracking accuracy runtime by jointly accounting for code loop tuning, front-end bandwidth, and received Carrier-to-Noise-density ratio (C/N_0).
Doppler measurements variance, instead, should account for the Phase-Lock Loop (PLL) carrier tracking jitter, influenced by thermal noise and short-term Allan deviation, and Frequency-Lock Loop (FLL) frequency tracking jitter, primarily affected by thermal noise, neglecting vibration-induced errors.
For a comprehensive understanding of each noise source, the reader is encouraged to refer to the literature on the topic (Kaplan and Hegarty, 2017).

III. METHODOLOGY

1. UKF architecture with orbital propagator

For non-linear transitional models, the sub-optimal EKF uses a Taylor series approximation under the Gaussian assumption for covariance prediction, while state-propagation can be achieved through numerical integration. In contrast, the UKF uses the Unscented Transform (UT) paradigm, which can directly capture the moments of a target Gaussian distribution, providing a more accurate representation of highly non-linear functions in sequential estimation. This section discusses the UKF model embedded with an orbital propagator for GNSS-based sequential OD. The EKF-based model is not extensively discussed, as it is well-documented in the literature (Capuano, 2016). However, the results section will evaluate both Bayesian models in the task of S/C orbital navigation in LLO, when GNSS observations are filtered in a tightly integrated configuration.

Following the augmented form of the UKF (Särkkä and Svensson, 2023) with process noise terms, the augmented posterior state estimate at t_{k-1} is expressed[4] as:

$$\hat{\boldsymbol{x}}^a_{k-1} = \begin{bmatrix} \hat{\boldsymbol{x}}^T_{k-1} \; \mathbf{0}_{1\times n} \end{bmatrix}^T . \tag{20}$$

Correspondingly, the augmented posterior covariance estimate follows as:

$$\hat{\boldsymbol{P}}^a_{k-1} = \begin{bmatrix} \hat{\boldsymbol{P}}_{k-1} & \mathbf{0}_{n\times n} \\ \mathbf{0}_{n\times n} & \boldsymbol{Q}_k \end{bmatrix} . \tag{21}$$

A set of $2n+1$ sigma-points are then deterministically computed as:

$$\boldsymbol{\chi}^i_{k-1} = \left[\left(\boldsymbol{\chi}^{i,\boldsymbol{x}}_{k-1} \right)^T \; \left(\boldsymbol{\chi}^{i,\boldsymbol{w}}_{k-1} \right)^T \right]^T = \begin{cases} \boldsymbol{\chi}^0_{k-1} = \hat{\boldsymbol{x}}^a_{k-1} & \text{for } \; i = 0 \\ \boldsymbol{\chi}^i_{k-1} = \hat{\boldsymbol{x}}^a_{k-1} + \sqrt{(n+\lambda) \left[\hat{\boldsymbol{P}}^a_{k-1} \right]_i} & \text{for } \; i = 1, \ldots, n \\ \boldsymbol{\chi}^{i+n}_{k-1} = \hat{\boldsymbol{x}}^a_{k-1} - \sqrt{(n+\lambda) \left[\hat{\boldsymbol{P}}^a_{k-1} \right]_i} & \text{for } \; i = n+1, \ldots, 2n \end{cases} \tag{22}$$

[3]When processing subcarrier modulated codes, the modified formulation discussed in (Betz, 2000) should be used. Yet for the processing of Galileo E5 and E5ab signals, code tracking error models can be found in (Tawk et al., 2012).

[4]For discrete-time equivalent models, the additive discrete process sequence has the same dimensionality of the state vector. However, this is not true in general, and a similar equivalence does not hold for model noises defined directly in discrete time (Gustafsson and Gustafsson, 2000)

where $[\cdot]_i$ denotes the i-th matrix column, and the square-root of a matrix is computed from the Cholesky decomposition of the positive definite $\hat{\boldsymbol{P}}^a_{k-1}$. The terms of $\boldsymbol{\chi}^i_{k-1}$ can be further decomposed as:

$$\boldsymbol{\chi}^{i,\boldsymbol{x}}_{k-1} = \left[\left(\boldsymbol{\chi}^{i,sc}_{k-1}\right)^T \ \left(\boldsymbol{\chi}^{i,clk}_{k-1}\right)^T\right]^T \ ; \ \boldsymbol{\chi}^{i,\boldsymbol{w}}_{k-1} = \left[\boldsymbol{0}_{1\times 3} \ \left(\boldsymbol{\chi}^{i,\boldsymbol{w}^{sc}}_{k-1}\right)^T \ \left(\boldsymbol{\chi}^{i,\boldsymbol{w}^{clk}}_{k-1}\right)^T\right]^T \tag{23}$$

to differentiate between the components relative to S/C positioning states and those relative to the GNSS receiver clock. Equation (22) defines the scaled UT (Van Der Merwe, 2004) with

$$\lambda = \alpha^2 (n+\kappa) - n \tag{24}$$

determining the spread of the sigma-points around the mean of the posterior state density; this spread is tuned through the filter parameters (α, κ). The sigma-points are assigned a set of scalar, time-invariant weights:

$$W_i = \begin{cases} \frac{\lambda}{n+\lambda} & i = 0 \\ \frac{1}{2(n+\lambda)} & i = 1, \dots, 2n \end{cases} \tag{25}$$

a) Moments of the Gaussian prior state density

$$\begin{aligned} \hat{\boldsymbol{x}}^-_k &= \sum_{i=0}^{2n} W_i \boldsymbol{\chi}^{i,\boldsymbol{x}}_{k|k-1} \\ \hat{\boldsymbol{P}}^-_k &= \sum_{i=0}^{2n} W_i \left[\boldsymbol{\chi}^{i,\boldsymbol{x}}_{k|k-1} - \hat{\boldsymbol{x}}^-_k\right] \left[\boldsymbol{\chi}^{i,\boldsymbol{x}}_{k|k-1} - \hat{\boldsymbol{x}}^-_k\right]^T . \end{aligned} \tag{26}$$

The term $\boldsymbol{\chi}^{i,\boldsymbol{x}}_{k|k-1}$ is obtained through numerical integration of $\left(\boldsymbol{\chi}^{i,sc}_{k-1}, \boldsymbol{\chi}^{i,\boldsymbol{w}^{sc}}_{k-1}\right)$ based on (9), and linear propagation of $\left(\boldsymbol{\chi}^{i,clk}_{k-1}, \boldsymbol{\chi}^{i,\boldsymbol{w}^{clk}}_{k-1}\right)$ via (12). The predicted covariance evaluates the spread of the time propagated sigma-points over the estimated mean of the prior. For the i-th time-propagated sigma-point $\boldsymbol{\chi}^{i,\boldsymbol{x}}_{k|k-1}$, the predicted GNSS measurement vector $\hat{\boldsymbol{z}}^i_k$ is calculated by leveraging the non-linear functional models (10) and (11). The predicted GNSS measurement vector would then be computed:

$$\hat{\boldsymbol{z}}_k = \sum_{i=0}^{2n} W_i \hat{\boldsymbol{z}}^i_k \tag{27}$$

b) Posterior estimation

$$\begin{aligned} \boldsymbol{P}_{\boldsymbol{xz}} &= \sum_{i=0}^{2n} W_i \left[\boldsymbol{\chi}^{i,\boldsymbol{x}}_{k|k-1} - \hat{\boldsymbol{x}}^-_k\right] \left[\hat{\boldsymbol{z}}^i_k - \hat{\boldsymbol{z}}_k\right]^T \\ \boldsymbol{P}_{\boldsymbol{zz}} &= \sum_{i=0}^{2n} W_i \left[\hat{\boldsymbol{z}}^i_k - \hat{\boldsymbol{z}}_k\right] \left[\hat{\boldsymbol{z}}^i_k - \hat{\boldsymbol{z}}_k\right]^T \\ \hat{\boldsymbol{x}}_k &= \hat{\boldsymbol{x}}^-_k + \boldsymbol{P}_{\boldsymbol{xz}} \boldsymbol{P}^{-1}_{\boldsymbol{zz}} (\boldsymbol{z}_k - \hat{\boldsymbol{z}}_k) \\ \hat{\boldsymbol{P}}_k &= \hat{\boldsymbol{P}}^-_k - \boldsymbol{P}_{\boldsymbol{xz}} \boldsymbol{H}^T_k - \boldsymbol{H}_k \boldsymbol{P}^T_{\boldsymbol{xz}} + \boldsymbol{H}_k \boldsymbol{P}_{\boldsymbol{zz}} \boldsymbol{H}^T_k \end{aligned} \tag{28}$$

where $\boldsymbol{z}_k$ is the GNSS measurement vector at the sample instant (cf. Section II.2), $\boldsymbol{P}_{\boldsymbol{xz}}$ is the the cross-covariance between $\hat{\boldsymbol{x}}^-_k$ and $\hat{\boldsymbol{z}}_k$, and $\boldsymbol{P}_{\boldsymbol{zz}}$ is the innovation covariance (Julier et al., 2000). The last relation of (28) expresses a generalized Joseph formula for the posterior covariance estimation, applicable to non-linear measurement models (Zanetti and DeMars, 2013).

2. Lunar orbit scenario

The upcoming LuGRE mission is considered as case-study to assess the potential of more complex non-linear Bayesian formulations when tackling the challenges of autonomous orbital navigation of a S/C in the lunar regime.

The initial state-vector of the BGM1 lander has been used in Ansys Systems Tool Kit (STK) to retrieve ephemeris parameters for the whole mission based on the High Precision Orbit Propagator (HPOP). The ephemeris parameters are expressed in the

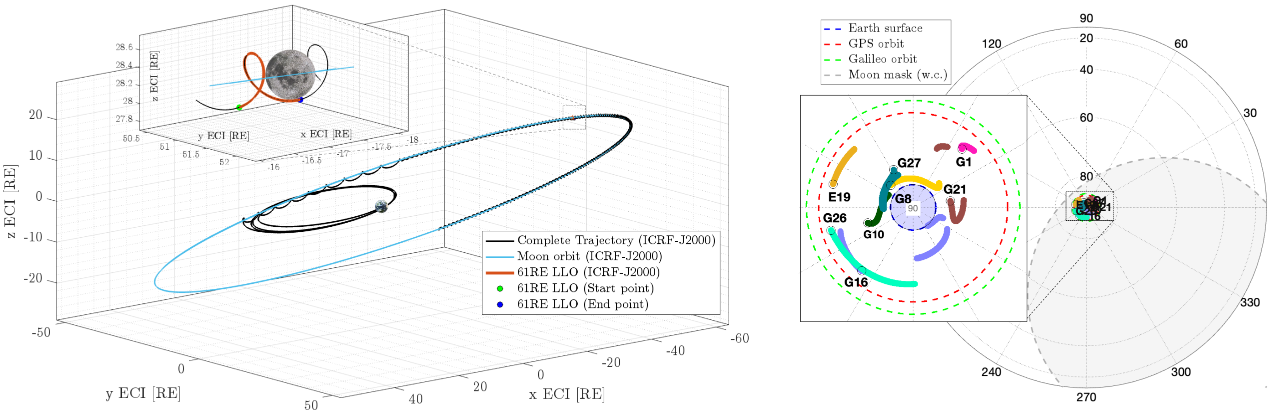

(a) (b)

Figure 2: (a) The BGM1 lander trajectory with a zoom in the analyzed LLO segment. (b) The dynamic skyplot of tracked GPS and Galileo satellites in lunar proximity.

Table 1: Overview of the analyzed LuGRE mission segment in LLO.

Parameter	Value
Trajectory Type	LLO
Reference Frame	ICRF (ECI-J2000 realization)
Initial geocentric distance [km] (RE)	389032.47 (60.99)
Maximum geocentric distance [km] (RE)	390981.82 (61.30)
Mean geocentric distance [km] (RE)	389206.46 (61.02)
Initial GPS time [s] / UTCG date	1411329668.38 / 25-Sep-2024 20:01:49.382
Final GPS time [s] / UTCG date	1411336800.38 / 25-Sep-2024 21:59:42.382
Sampling time [s]	60

geocentric, inertial J2000 frame, and are converted to position and velocity states. Starting from the complete mission trajectory (45.97 days), a section (2 hours) has been selected for the evaluation of the navigation algorithms. This section has been chosen because it reflects the mission's scientific objectives and is characterized by particularly challenging navigation conditions, including limited availability of satellite measurements and degraded geometry. It involves a selenocentric segment in LLO around 61 Earth Radii (RE) and close to apolune, happening after the second Lunar Orbit Injection (LOI) maneuver (Parker et al., 2022). The LuGRE trajectory together with the analyzed LLO section are shown in Figure 2(a). Moreover, the LLO details are summarized in Table 1. For the selected LLO, the original 60-second step trajectory was up-sampled to 1 Hz performing 7-th order Lagrange interpolation in General Mission Analysis Tool (GMAT) (Hughes et al., 2014). This step was performed in view of emulating the operational scenario of the LuGRE receiver (cf. Section III.3). Eventually, a frame transformation to an Earth-fixed frame (ECEF-WGS84 realization) was operated on the up-sampled trajectory segment by accounting for Earth's rotational effects relative to inertial space.

The reported trajectory is based on pre-launch orbit design and does not reflect the actual trajectory the BGM1 lander will follow upon deployment. Details of the operational orbit remain undisclosed.

3. RF simulation framework & navigation analysis

To emulate the GNSS operational environment and the RF signal conditions the LuGRE receiver is expected to be subject to in the LLO segment, a multi-GNSS simulation model was configured in Spirent GSS9000 GNSS RF simulator (Spirent, 2015). Consistent with the NEIL hardware design and Earth GNSS signal processing capabilities, only GPS (G) and Galileo (E) constellations were modelled in the simulation environment. The most recent Almanac data and space-segment operational advisories were incorporated into the navigation systems' configuration. Although also other services are broadcast by the respective satellite payloads, the RF signal generation was confined to L1 C/A and L5 signals for GPS, and E1 and E5a signals for Galileo. For the Global Positioning System (GPS) constellation, the gain patterns of batches IIR and IIR-M were modelled according to (Marquis, 2016), with the boresight EIRP configured based on (Delépaut et al., 2020) for L1 C/A and L5-Q signals. Similarly, the gain pattern for batch IIF was taken from (Donaldson et al., 2020), and replicated for batch III-A. For the Galileo

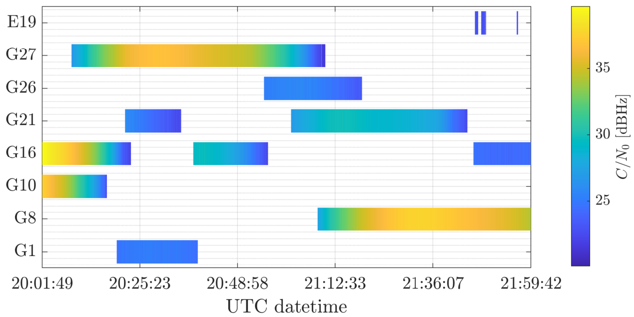

(a) C/N_0 from RF-visible satellites (L1/E1)

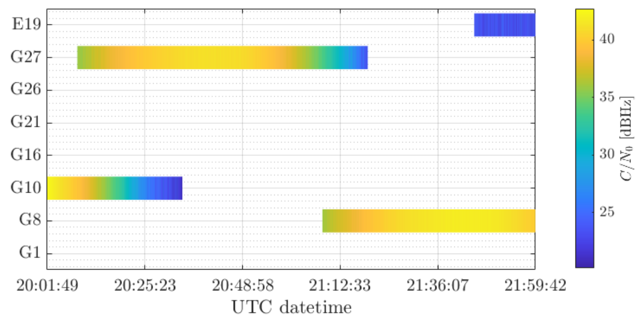

(b) C/N_0 from RF-visible satellites (L5/E5a)

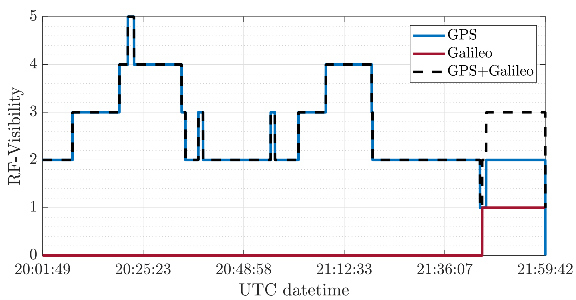

(c) Visibility map of GNSS satellites (unique SVs)

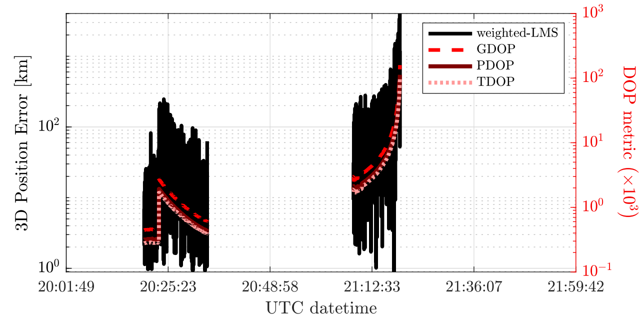

(d) Single-point positioning error (left axis) and Dilution of Precision metrics (right axis).

Figure 3: GNSS environment seen by the LuGRE receiver in the analyzed LLO segment in terms of relevant navigation metrics.

constellation, instead, patterns were configured based on the reference model for first generation Full Operational Capability (FOC) satellite antennas (Menzione et al., 2024). Moreover, the non-isotropic radiation patterns of both GNSS systems for the modelled signals were truncated with an off-boresight mask to account for satellite body effects. Further insights about RF link simulation can be found in (Tedesco et al., 2023).

Regarding atmospheric effects, GNSS signals received from satellites on the opposite side of the Earth relative to the S/C's position cross the ionosphere twice, causing greater delays and introducing unmodelled biases in the retrieved measurements. These signals correspond to the main lobe portion in the transmitting EIRP that spills over the Earth's disk and is confined within the altitude of the ionospheric layer (i.e., $\approx 10^3$ km). For GPS satellites, this translates to an angle of approximately $13°$ in the EIRP pattern, with an additional $2.2°$ margin for the ionosphere, while for Galileo satellites, the angles are slightly smaller at approximately $12°$ plus $2°$ respectively, due to the higher orbit radius. At Moon altitudes, the likelihood of receiving such signals is very low, as demonstrated in the feasibility study by (Delépaut et al., 2020). Therefore, ionospheric effects were neglected in the simulation, which is justified for the analyzed LLO section of the LuGRE trajectory. Nevertheless, when tracking dual-band signals for the same satellite and processing observables, ionospheric-free measurements can be obtained, albeit with higher noise variance.

Based on the described framework, a HIL test was conducted by integrating the NEIL receiver in the configured GNSS testbench. Digitally generated signals for GPS L1/L5 and Galileo E1/E5a bands were upconverted to RF and transmitted through Spirent's Signal Generator Unit (SGU). RF signals were eventually processed by the LuGRE receiver, thus allowing the record and post-processing of dual-band raw measurements from both constellations.

Figure 2(b) displays the dynamic skyplot of GPS and Galileo satellites, whose signals are tracked and for which observables are constructed, according to the high-sensitivity acquisition and tracking capabilities of the LuGRE receiver. This polar diagram considers the instantaneous relative dynamics between the S/C and the tracked GNSS satellites in the LLO segment. The positions and velocities of the tracked GNSS satellites are projected onto a Local Vertical Local Horizontal (LVLH) frame (for Space Data Systems , CCSDS), with the radial direction representing the S/C's boresight, assuming perfect pointing to the Earth's center of mass. To ease graphical interpretation, a zoom is included that frames the boresight direction; it is clearly visible that the batch of tracked satellites is clustered at boresight thus lacking variability in elevation due to the large distance of the S/C from the Earth compared to the GPS/Galileo orbit semi-major axis. Moreover, the minimum elevation for the Earth's disk and the elevation isolines of both GPS and Galileo systems are identified by modeling the GNSS system's orbit semi-major axis and flattening. For each S/C position, an ellipsoid is considered, and the minimum elevation level is determined and repeated over the entire analyzed LLO. This elevation isoline represents the boundary circle beyond which satellites cannot be seen inside the polar diagram. The Moon's occlusion of the S/C-to-Earth LOS is considered as well instant-by-instant, with the skyplot representing the worst-case Moon occupation. Despite this occlusion, RF signals are not necessarily blocked. Given the S/C's mean geocentric distance (cf. Table 1) and the Moon's radius (about 0.2727 of Earth's mean equatorial radius), the Moon's disk occupies an angle roughly 84.19 times smaller than the Galileo E1 main lobe beamwidth when the Moon center of mass is taken collinear with the S/C-to-Earth LOS.

By setting a 20 dB-Hz threshold as the minimum received C/N_0 level of a signal for the corresponding raw observable to be considered available for processing in the PVT unit, the C/N_0 patterns seen by the LuGRE receiver are depicted in Figure 3(a) for L1/E1 band and in Figure 3(b) for the L5/E5a band. For the mean geocentric distance of the analyzed LLO, a 30 dB-Hz threshold is reasonable to differentiate between the reception of the main lobe and peak side lobes. The measured C/N_0 levels for L5/E5a band signals are higher, reaching up to 43 dB-Hz for GPS L5, due to the wider transmission pattern beamwidth and lower path loss. This aligns with the observations by (Delépaut et al., 2020). However, more signals are tracked on the L1/E1 band because only a subset of satellites of each system broadcasts services in the lower frequency band. Notably, measurements are available from only one Galileo satellite (i.e., E19) in the whole LLO segment, with a side lobe signal being tracked. This is likely caused by the conservative modeling of Galileo EIRP in the simulator, or the orbital geometry, as Galileo satellites are distributed across three orbital planes compared to GPS's six, limiting orbital diversity.

Figure 3(c) illustrates the radiometric visibility profile of GNSS satellites throughout the entire LLO section. It shows that a maximum of five GPS satellites are tracked for a short interval of 130 s, accounting for only the 1.21% of the dataset length. On average, 2.72 satellites are tracked, indicating that fewer than three satellites are available for most of the dataset. Moreover, the availability of the minimum number of measurements required for the computation of a single-point PVT solution is 21.32%. This availability is reflected in the weighted Least-Mean Squares (LMS) solution shown in Figure 3(d) (left axis). The right axis on the same figure highlights the profiles of geometric DOP (GDOP), position DOP (PDOP), and time DOP (TDOP). To better illustrate the dependence of the single-point positioning error on the DOP metrics, a logarithmic scale was chosen. Due to the scarcity of tracked GNSS satellites, the LLO scenario is characterized by remarkable DOP discontinuities. In particular, the rapidly changing geometric conditions can be characterized by steep ascending ramps, which rapidly deteriorate the accuracy of GNSS single-point estimates.

IV. RESULTS

This section discusses the OD performance of the UKF-based OF model (cf. Section III.1) within the analyzed LLO scenario in the LuGRE framework, benchmarked against the renowned EKF-based model. The filtering-based algorithms are analyzed for post-processing sampled GNSS observations collected by the LuGRE receiver in the HIL simulation (cf. Section III.3). The filters have been developed with equivalent orbital propagators modeling S/C dynamics, and share the same stochastic characterization of the noises affecting both the process and the measurements (cf. Section II.3). It is remarked that sequential estimators require an initial condition for the PVT states, which models the prior knowledge about the system. Typically, this initialization can be provided through a (weighted) single-point solution. However, the limited multi-system, multi-channel position fixing availability observed in lunar proximity (cf. Figure 3) suggests the need for alternative approaches. For the current assessment, aided initialization is assumed; in the real operational scenario, this approach would leverage data via the ground-based TeleCommand (TC) link. Similarly, in this analysis, the navigation algorithms are initialized using the upsampled BGM1 lander trajectory. To simulate inaccuracies in the aiding information, purposely degraded initialization is considered. For the position states, a $10^3\ \mathrm{m}$ error is uniformly added to each spatial dimension. A similar approach is applied to the velocity states, with a smaller error accounting for the $0.1\ \%$ of the true lander speed at the initial sample time. In the absence of reference values for the receiver timing states, approximate values of $10^3\ \mathrm{m}$ and $10^{-4}\ \mathrm{m\,s^{-1}}$ are assigned, and this lack of prior knowledge is modelled in the covariance of the initial state distribution.

Figure 4 shows the time-series of S/C position and velocity estimation errors (ECI frame) using dual-channel GNSS observations, with separate plots for position (Figure 4(a)) and velocity (Figure 4(b)). The solid lines of each error subplot evaluate the distance of the estimated mean of the posterior density from the true lander positioning state at the sample instant. Moreover, the shaded areas indicate the conditional 3-sigma Root-Sum-Squared (RSS) error. Figure 5 presents the errors in the S/C comoving orbital frame, separating radial error from the orthogonal plane components. Cumulative error statistics are summarized in Table 2.

Upon the biased initialization of $10^3\ \mathrm{m}$, the radial position error in Figure 5(a) reduces to about $50\mathrm{m}$ after the first sample of GNSS observations are filtered through to orbital propagator. Given that the tracked satellites are clustered at high elevation (cf. 2(b)), the radial error mirrors the error in the receiver clock offset estimate. A similar behavior characterizes the radial component of the velocity estimate, as shown in Figure 5(b). Despite the limited number of available measurements at the beginning of the LLO section, the receiver timing states possess enough observability to allow for the convergence of the radial estimate. Conversely, the normal component exhibits an error bigger than the initial mismatch and takes longer time (about 10

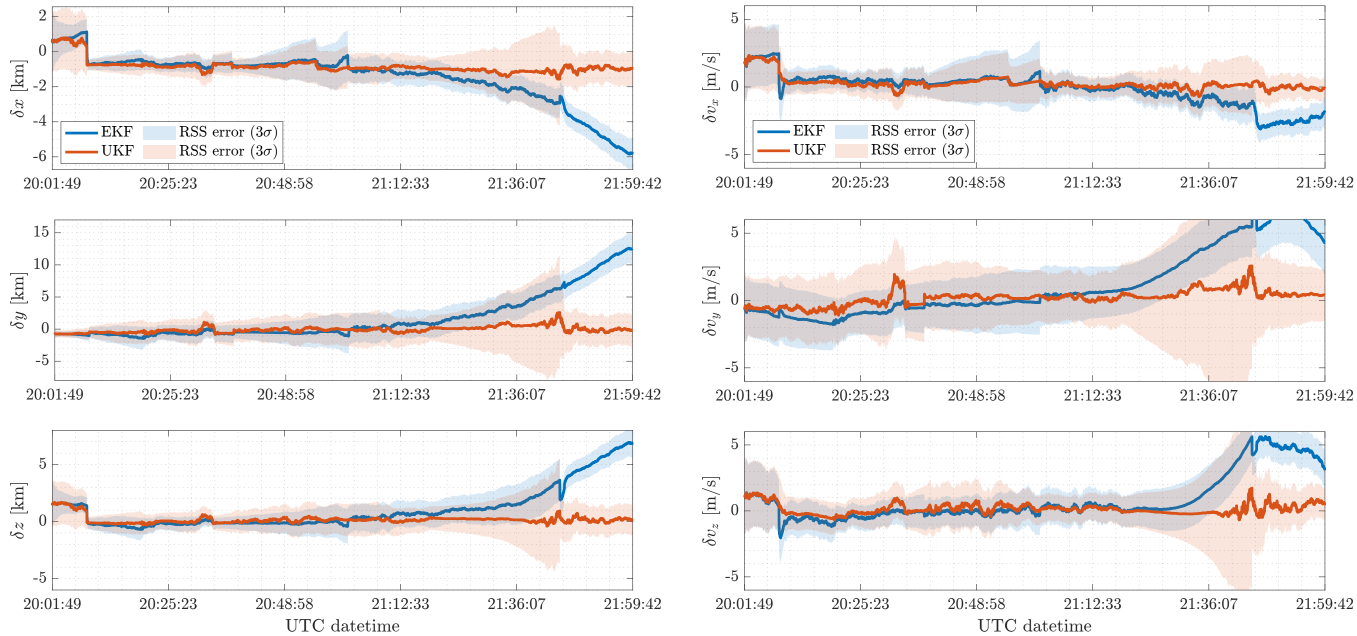

(a) Axial Position Error (ECI frame)

(b) Axial Velocity Error (ECI frame)

Figure 4: EKF and UKF OD error (solid line) with RSS confidence intervals (shaded area) at 3σ (99.7% confidence).

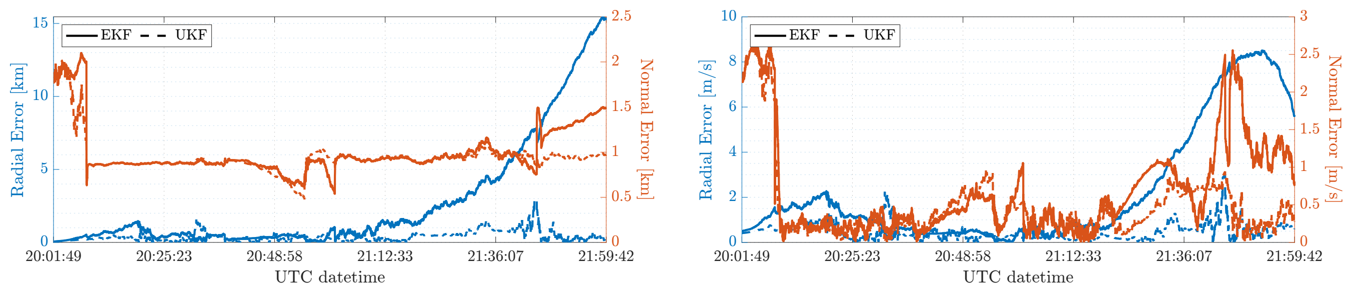

(a) Position (RIC frame)

(b) Velocity (RIC frame)

Figure 5: EKF and UKF OD error decomposed in radial (left axis) and normal (right axis) components of a local orbital frame.

minutes) to reduce for both filters. Additionally, for the normal components, the mean posterior estimates remain biased by roughly the same amount as the simulated initialization error. This suggests that accurate initialization is crucial for achieving accurate OD solutions in operational scenarios with significant depletion of Earth GNSS signal, such as those experienced at the Moon.

During the first time frame of single-point PVT availability (cf. Figure 3(d) between 20:20 and 20:34), the radial position and velocity error profiles of both estimators follow the GDOP pattern as expected. However, at the end of the time frame, the UKF radial position estimate exhibits a sudden deviation while the EKF remains stable. This phenomenon might be associated with a decrease in the observability of the clock states due to the loss of L1 signal track for satellites G1 and G21 (cf. Figure 3(a)), along with the UKF filter gain weighting more the observations than the EKF. Moreover, examining the entire LLO section, abrupt variations in the radial error time series often coincide with discontinuities in the radiometric tracking of satellites (cf. Figure 3(c)). These discontinuities can determine anomalies in the clock states' estimates, directly affecting the radial terms. However, the UKF appears to be less affected by these effects, resulting in a smoother estimate overall.

More interesting effects can be observed during the second time frame of single-point PVT availability (cf. Figure 3(d) between 21:8 and 21:19), which is marked by a harmful PDOP ramp with values reaching nearly 160×10^3. At the end of this ramp, coinciding with the loss of signal track for G1 on L1 band and G7 on L5, the conditional posterior estimates from the two filters highlight different behaviors. the EKF posterior mean for both position and velocity states drifts, accumulating an error against the true lander state that increases exponentially over time. This is clearly evidenced by the axial errors in Figure 4.

Table 2: Cumulative OD error statistics for EKF and UKF architectures.

Bayesian Filter	Position Error [km]				Velocity Error [m/s]			
	68.3%	95.5%	99.7%	100%	68.3%	95.5%	99.7%	100%
EKF	2.26	13.06	15.43	15.52	2.42	8.44	8.63	8.67
UKF	1.02	1.76	3.09	3.16	0.81	2.29	3.14	3.20

Despite the growing error, the EKF maintains high confidence in its estimate, as the 3σ RSS error profile closely follows the OD error curves. This likely results from the non-linearity of the system dynamics, which compromises the validity of the EKF Taylor approximation about the latest state estimate. For each component of $\boldsymbol{x}_k^{sc}$, comparing the terms of (15) evaluated both about the latest state estimate and about the true lander state, the difference between these quantities exceeds the corresponding state estimate's uncertainty, leading to an overoptimistic covariance and a growing state estimation error. Conversely, the UKF posterior estimate maintains its accuracy, albeit the above mentioned bias on the normal component. Simultaneously, the UKF confidence in the estimate decreases exponentially, as indicated by the RSS error profile. This suggests that the UT-based approximation of the state density better accounts for unknown changes in the system dynamics in the absence of GNSS observations. Moreover, sigma-points enable an improved approximation of state correlations in the Gaussian belief, which is crucial for maintaining estimate quality under compromised state observability. In the final part of the LLO, new measurements from a Galileo satellite allow for a reduction in the UKF state uncertainty estimate. For the EKF, instead, the estimate is sensitive to changes in the observables' set, but this is insufficient to recover from divergence.

V. CONCLUSION

This study has demonstrated the performance of autonomous GNSS-based OD in the lunar regime. In a sequential Bayesian architecture which integrates GNSS radiometric observations tightly with the prediction of space dynamics from an orbital propagator, the potential of an UKF-based model has been investigated for statistical OD. The more complex sigma-point filter has been compared against the renown EKF-based OF model, showcasing near-Moon PNT at about 61 RE. The upcoming LuGRE scientific mission has served as case-study, selecting a LLO segment from a pre-launch design of the BGM1 trajectory. Both Bayesian navigation algorithms have been assessed through the post-processing of raw multi-band GPS/Galileo observables; these measurements have been constructed by the NEIL receiver in a HIL test with realistic RF link simulation.

By leveraging the UT under the Gaussian assumption, the UKF can better approximate the moments of the posterior belief for the latent state. When the state observability is undermined due to the absence of fresh measurements, enhanced OD performance can be pursued through better modelling the correlations of states while propagating orbital dynamics. This seems promising in scenarios with severe satellite signal depletion, such as in lunar proximity. Moreover, the UKF's sigma-point sampling proves effective in maintaining estimate accuracy and mitigating the effects of harmful discontinuities characterizing multi-lateration geometry in the lunar regime.

Highlights of the study include:

- The UKF maintains position estimation errors within $2\ \mathrm{km}$ for the 98.97% of time over the analyzed dataset, with a net 3σ accuracy gain over the EKF of 79.97% for the position estimate and of 63.62% for the velocity estimate.
- Under detrimental GDOP conditions, the UKF results in a smoother and more resilient state estimate compared to the EKF; the latter exhibits a divergent trend driven by an overoptimistic covariance estimate.
- Accurate initialization might be critical for both filters, particularly in the lunar environment, where availability of radiometric observations is limited and mismatching biases can be hardly cancelled.
- The strong yet peculiar TDOP caused by the lack of elevation diversity in satellite ranging sources necessitates sequential estimators that can reduce the sensitivity of radial estimates to discontinuities in the timing estimates.

Aligning with the goals of increased autonomy, the UKF-based OF model seems to offer a promising solution for GNSS-based onboard OD in the lunar regime. Further research will aim to further enhance PNT algorithms, and GNSS-based OD will be explored in different deep-space and cis-lunar operational scenarios.

ACKNOWLEDGEMENTS

This study was funded within the contract n. 2021-26-HH.0 ASI/Politecnico di Torino ”Attività di R&S inerente alla Navigazione GNSS nello Space volume Terra/Luna nell'ambito del Lunar GNSS Receiver Experiment”. O. Vouch acknowledges funding from the Politecnico di Torino Interdepartmental Centre for Service Robotics (PIC4SeR). A. Minetto acknowledges funding from the research contract no. 32-G-13427-5 DM 1062/2021 funded within the Programma Operativo Nazionale (PON) Ricerca ed Innovazione of the Italian Ministry of University and Research (MUR).

REFERENCES

Bar-Shalom, Y., Li, X. R., and Kirubarajan, T. (2004). *Estimation with applications to tracking and navigation: theory algorithms and software*. John Wiley & Sons.

Battin, R. H. (1999). *An introduction to the mathematics and methods of astrodynamics*. Aiaa.

Betz, J. W. (2000). Design and performance of code tracking for the gps m code signal. In *Proceedings of the 13th International Technical Meeting of the Satellite Division of The Institute of Navigation (ION GPS 2000)*, pages 2140–2150.

Betz, J. W. and Kolodziejski, K. R. (2000). Extended theory of early-late code tracking for a bandlimited gps receiver. *Navigation*, 47(3):211–226.

Brown, R. G. and Hwang, P. Y. (1992). Introduction to random signals and applied kalman filtering(book). *New York, John Wiley & Sons, Inc., 1992. 512*.

Capuano, V. (2016). Gnss-based navigation for lunar missions. Technical report, EPFL.

Capuano, V., Shehaj, E., Botteron, C., Blunt, P., and Farine, P.-A. (2017). Keynote: An adaptive gnss-based reduced dynamic approach for real time autonomous navigation from the earth to the moon. In *Proceedings of the ION 2017 Pacific PNT Meeting*, pages 331–347.

Delépaut, A., Giordano, P., Ventura-Traveset, J., Blonski, D., Schönfeldt, M., Schoonejans, P., Aziz, S., and Walker, R. (2020). Use of gnss for lunar missions and plans for lunar in-orbit development. *Advances in Space Research*, 66(12):2739–2756.

Donaldson, J. E., Parker, J. J., Moreau, M. C., Highsmith, D. E., and Martzen, P. D. (2020). Characterization of on-orbit gps transmit antenna patterns for space users. *NAVIGATION, Journal of the Institute of Navigation*, 67(2):411–438.

Fang, H., Tian, N., Wang, Y., Zhou, M., and Haile, M. A. (2018). Nonlinear bayesian estimation: From kalman filtering to a broader horizon. *IEEE/CAA Journal of Automatica Sinica*, 5(2):401–417.

for Space Data Systems (CCSDS), C. C. (2019). *CCSDS Report Concerning Navigation Data—Definitions and Conventions*. Washington, DC, USA, issue 4 edition. Green Book, Informational Report.

Galleani, L. (2008). A tutorial on the two-state model of the atomic clock noise. *Metrologia*, 45(6):S175.

Gustafsson, F. and Gustafsson, F. (2000). *Adaptive filtering and change detection*, volume 1. Wiley New York.

Hughes, S. P., Qureshi, R. H., Cooley, S. D., and Parker, J. J. (2014). Verification and validation of the general mission analysis tool (gmat). In *AIAA/AAS astrodynamics specialist conference*, page 4151.

Iess, L., Di Benedetto, M., James, N., Mercolino, M., Simone, L., and Tortora, P. (2014). Astra: Interdisciplinary study on enhancement of the end-to-end accuracy for spacecraft tracking techniques. *Acta Astronautica*, 94(2):699–707.

Iiyama, K., Bhamidipati, S., and Gao, G. (2024). Precise positioning and timekeeping in a lunar orbit via terrestrial gps time-differenced carrier-phase measurements. *NAVIGATION: Journal of the Institute of Navigation*, 71(1).

Julier, S., Uhlmann, J., and Durrant-Whyte, H. F. (2000). A new method for the nonlinear transformation of means and covariances in filters and estimators. *IEEE Transactions on automatic control*, 45(3):477–482.

Kaplan, E. and Hegarty, C. (2017). *Understanding GPS/GNSS: Principles and Applications*. Artech House.

Marquis, W. (2016). The gps block iir antenna panel pattern and its use on-orbit. In *Proceedings of the 29th International Technical Meeting of the Satellite Division of The Institute of Navigation (ION GNSS+ 2016)*, pages 2896–2909.

McMahon, J. W. (2011). *An analytical theory for the perturbative effect of solar radiation pressure on natural and artificial satellites*. PhD thesis, University of Colorado at Boulder.

Menzione, F., Sgammini, M., Paonni, M., et al. (2024). Reconstruction of galileo constellation antenna pattern for space service volume applications. *Publications Office of the European Union: Luxembourg*.

Minetto, A., Dovis, F., Nardin, A., Vouch, O., Impresario, G., and Musmeci, M. (2022). Analysis of GNSS data at the Moon for the LuGRE project. In *2022 IEEE 9th International Workshop on Metrology for AeroSpace (MetroAeroSpace)*, pages 134–139. ISSN: 2575-7490.

Montenbruck, O., Gill, E., and Lutze, F. (2002). Satellite orbits: models, methods, and applications. *Appl. Mech. Rev.*, 55(2):B27–B28.

Morichi, L., Minetto, A., Nardin, A., Zocca, S., and Dovis, F. (2024). Pseudorange and doppler-based state estimation from meo to leo: A comprehensive analysis of maximum likelihood estimators. In *Proceedings of the 2024 International Technical Meeting of The Institute of Navigation*, pages 677–691.

Murata, M. (2023). Ensemble kalman filter for moon transfer orbit gps navigation. In *Proceedings of the 2023 International Technical Meeting of The Institute of Navigation*, pages 204–212.

Nardin, A., Minetto, A., Guzzi, S., Dovis, F., Konitzer, L., and Parker, J. J. K. (2023). Snapshot tracking of GNSS signals in space: A case study at lunar distances. In *Proceedings of the 36th International Technical Meeting of the Satellite Division of The Institute of Navigation (ION GNSS+ 2023)*, pages 3267–3281, Denver, Colorado.

Nardin, A., Minetto, A., Vouch, O., Maiani, M., and Dovis, F. (2022). Snapshot acquisition of GNSS signals in space: a case study at lunar distances. In *Proceedings of the 35th International Technical Meeting of the Satellite Division of The Institute of Navigation (ION GNSS+ 2022)*, pages 3603 – 3617, Denver, Colorado.

Park, R. S., Folkner, W. M., Williams, J. G., and Boggs, D. H. (2021). The jpl planetary and lunar ephemerides de440 and de441. *The Astronomical Journal*, 161(3):105.

Parker, J. J., Bauer, F. H., Ashman, B. W., Miller, J. J., Enderle, W., and Blonski, D. (2018). Development of an interoperable gnss space service volume. In *Proceedings of the 31st International Technical Meeting of the Satellite Division of The Institute of Navigation (ION GNSS+ 2018)*, pages 1246–1256.

Parker, J. J., Dovis, F., Anderson, B., Ansalone, L., Ashman, B., Bauer, F. H., D'Amore, G., Facchinetti, C., Fantinato, S., Impresario, G., et al. (2022). The Lunar GNSS Receiver Experiment (LuGRE). In *Proceedings of the 2022 International Technical Meeting of The Institute of Navigation (ION ITM 2022)*, pages 420–437.

Särkkä, S. and Svensson, L. (2023). *Bayesian filtering and smoothing*, volume 17. Cambridge university press.

Schutz, B., Tapley, B., and Born, G. H. (2004). *Statistical orbit determination*. Elsevier.

Spirent (2015). GSS9000 GNSS Simulator.

Tawk, Y., Botteron, C., Jovanovic, A., and Farine, P.-A. (2012). Analysis of galileo e5 and e5ab code tracking. *GPS solutions*, 16:243–258.

Tedesco, S., Bernardi, F., Guzzi, S., Boschiero, M., Pulliero, M., Marcantonio, D., Ghedin, M., Miotti, E., Fantinato, S., Pozzobon, O., et al. (2023). Deep space gnss in moon transfer orbit: the lugre receiver. In *2023 IEEE International Conference on Wireless for Space and Extreme Environments (WiSEE)*, pages 1–6. IEEE.

Teunissen, P. J. G. and Montenbruck, O. (2017). *Springer handbook of global navigation satellite systems*, volume 10. Springer.

Turan, E., Speretta, S., and Gill, E. (2022). Autonomous navigation for deep space small satellites: Scientific and technological advances. *Acta Astronautica*, 193:56–74.

Van Der Merwe, R. (2004). *Sigma-point Kalman filters for probabilistic inference in dynamic state-space models*. Oregon Health & Science University.

Vouch, O., Nardin, A., Minetto, A., Zocca, S., Valvano, M., and Dovis, F. (2024). Aided kalman filter models for gnss-based space navigation. *IEEE Journal of Radio Frequency Identification*, 8:535–546.

Zanetti, R. and DeMars, K. J. (2013). Joseph formulation of unscented and quadrature filters with application to consider states. *Journal of Guidance, Control, and Dynamics*, 36(6):1860–1864.